



Optical diffraction tomography from single-molecule localization microscopy

Thanh-an Pham^{a,*}, Emmanuel Soubies^b, Ferréol Soulez^c, Michael Unser^a

^a Biomedical Imaging Group, École polytechnique fédérale de Lausanne, Lausanne, Switzerland

^b IRT, Université de Toulouse, CNRS, Toulouse, France

^c Univ. Lyon, Univ. Lyon1, ENS de Lyon, CNRS, Centre de Recherche Astrophysique de Lyon, Saint-Genis-Laval, France



ARTICLE INFO

Keywords:

Computational imaging

Joint optimization

Refractive index reconstruction

Fluorescence microscopy

ABSTRACT

Single-molecule localization microscopy (SMLM) is a powerful method for the imaging of cellular structures. This modality delivers nanoscale resolution by sequentially activating a subset of fluorescent molecules and by extracting their super-resolved positions from the microscope images. The emission patterns of individual molecules can be distorted by the refractive-index (RI) map of the sample, which reduces the accuracy of the molecule localization if not accounted for. In this work, we show that one can exploit those sample-induced aberrations to reveal the structural information of the specimen. Our work is related to the optical diffraction tomography in that we aim to recover the RI map. To that end, we propose an optimization framework in which we reconstruct the RI map and optimize the positions of the molecules in a joint fashion. The benefits of our method are twofold. On one side, we effectively recover the RI map of the sample. On the other side, we further improve the molecule localization—the primary purpose of SMLM. We validate our joint-optimization framework on simulated data. Our results lay the foundation of an exciting and novel extension of SMLM.

1. Introduction

Single-molecule localization microscopy (SMLM) is a method of choice for the observation of biological phenomena at nanoscale resolution [1–3]. It breaks the diffraction limit of conventional fluorescence microscopy by sequentially activating and localizing a subset of fluorescent molecules. As such, SMLM is a prime example of computational microscopy where suitable acquisitions and algorithmic reconstruction are combined so as to enhance the capabilities of traditional systems. Although SMLM acquisitions are two-dimensional, innovative point-spread functions (PSF) whose shapes vary with depth have been designed to encode the axial position of molecules. These include the popular astigmatism [4] or double-helix [5] PSFs. Therefore, in addition to efficient localization algorithms, well-calibrated models of these PSFs are essential to reach the promised nanoscale resolution [6].

The standard practice is to estimate these PSFs from acquisitions of sub-resolved objects (e.g., fluorescent microspheres) [7,8]. However, this strategy ignores sample-induced distortions. Indeed, the heterogeneity of biological specimens—through variations in their refractive index (RI)—induces a scattering of the emitted light. This distorts the recorded emission patterns and compromises the accurate localization of molecules. To mitigate this effect, Xu et al. [9] proposed an algorithm to jointly localize fluorescent molecules and estimate an *in situ* PSF

model that has the ability to capture sample-induced aberrations and, hence, to improve localization accuracy.

If we could estimate both the RI and the position of molecules from the SMLM acquisition stack alone, then we would have a unique combination of structural (RI) and functional (fluorescence) information about the sample [10]. To our knowledge, such a reconstruction of both RI and fluorescence density from the same fluorescent dataset (*i.e.*, without phase measurements) has been investigated only recently by Xue and Waller [11]. They consider two-layers samples where the bottom layer contains fluorescence-labeled objects and the top layer contains non-labeled objects. In this context, they demonstrated that the 3D RI map of the non-labeled objects can be reconstructed from defocused fluorescence images that are collected by sequentially stimulating small regions of the fluorescence-labeled layer of the sample. Moreover, they showed that the obtained RI map can be exploited to obtain the scattered PSF and improve the fluorescence signal through deconvolution. This setting differs from the exploitation of the individual emission of fluorophores in SMLM that we propose here in two respects. First, RI and fluorescence objects are mixed (*i.e.*, no two-layers samples). Second, fluorescence measurements are recorded at two distinct focal planes (*i.e.*, biplane SMLM modality).

In SMLM, the recovery of the RI has been addressed in [12,13]. These two works exploit the fact that SMLM data can be seen as

* Corresponding author.

E-mail address: thanh-an.pham@epfl.ch (T.-a. Pham).

measurements of an optical-diffraction tomography (ODT) system with point-source illuminations inside the sample. In [12], the authors assumed that the phase of the measurements was accessible, an assumption which is not met in practice. Moreover, their proposed approach relies on a linear model whose validity is limited to weakly scattering samples [14]. In our preliminary work [13], we introduced a refined RI-reconstruction approach that can handle phaseless measurements under the assumption that the positions of the fluorescent molecules are perfectly known. This method is based on the exact (nonlinear) Lippmann–Schwinger equation.

1.1. Contributions and roadmap

In this work, we extend [13] in two ways. First, we consider a more realistic image-formation model (described in Section 2) that integrates background fluorescence as well as the shot noise inherent to fluorescence microscopy. Second, and more importantly, we consider that the positions of the molecules are known only approximately, as opposed to [13], and then take advantage of our model-based scheme to refine them.

To cope with this more challenging scenario, we propose a joint-optimization framework in Section 3. Our method simultaneously reconstructs the RI and refines the positions and amplitudes of the molecules. The benefits of our framework are twofold. On one side, we are accurately estimating the structural information (RI) from SMLM acquisitions. On the other side, we significantly improve the localization of the molecules—the primary objective of SMLM. We validate our framework on simulated data in Section 4.

1.2. Notations

Scalar and continuously defined functions are denoted by italic letter (e.g., $k_b \in \mathbb{R}$, $u \in L_2(\mathbb{R})$). The complex conjugate of $v \in \mathbb{C}$ is denoted by v^* . Vectors and matrices are denoted by bold lowercase and bold uppercase letters, respectively (e.g., $\mathbf{x} \in \mathbb{R}^N$, $\mathbf{G} \in \mathbb{C}^{N \times N}$). The m th element of a vector $\mathbf{v} \in \mathbb{R}^M$ is denoted as v_m or $[\mathbf{v}]_m$. Similarly, the n th column of a matrix $\mathbf{X} \in \mathbb{R}^{M \times N}$ is denoted as \mathbf{x}_n or $[\mathbf{X}]_n$. The notation \mathbf{G}^H refers to the conjugate transpose of the matrix $\mathbf{G} \in \mathbb{C}^{N \times N}$. The matrix $\mathbf{I}_N \in \mathbb{R}^{N \times N}$ is the identity and $\text{diag}(\mathbf{f}) \in \mathbb{R}^{N \times N}$ is a diagonal matrix formed out of the entries of $\mathbf{f} \in \mathbb{R}^N$. The notation $\mathbf{1}_M = (1, 1, \dots, 1) \in \mathbb{R}^M$ stands for an M -length vector of ones. Similarly, $\mathbf{0}_M$ denotes a vector of M zeros. Finally, \odot and \oslash stand for the Hadamard product and the pointwise division, respectively.

2. Image-formation model

2.1. SMLM meets ODT

The space-varying refractive index of the sample under consideration is represented by the function $\eta : \Omega \rightarrow \mathbb{R}$ with $\Omega \subseteq \mathbb{R}^3$. The sample is populated with L fluorophores located at spatial position $\{\mathbf{x}_l \in \Omega\}_{l=1}^L$. Without loss of generality, we consider an SMLM acquisition stack where a single fluorophore is activated on each frame. Indeed, because fluorophores are incoherent sources, the image produced upon activation of multiple emitters is simply the sum of the individual contribution of each emitter [15].

When activated, the l th fluorophore at position $\mathbf{x}_l \in \Omega$ emits a spherical wave with intensity $a_l > 0$, which leads to

$$u_{\text{in}}(\mathbf{x}; \mathbf{x}_l, a_l) = a_l \frac{\exp(jk_b \|\mathbf{x} - \mathbf{x}_l\|_2)}{4\pi \|\mathbf{x} - \mathbf{x}_l\|_2}, \quad (1)$$

where j is the imaginary unit and $k_b = \frac{2\pi\eta_b}{\lambda}$ is the wavenumber determined by the emission wavelength λ and the RI $\eta_b > 1$ of the surrounding medium. The spherical wave acts as an “incident” field that illuminates from within the sample. As such, it scatters through

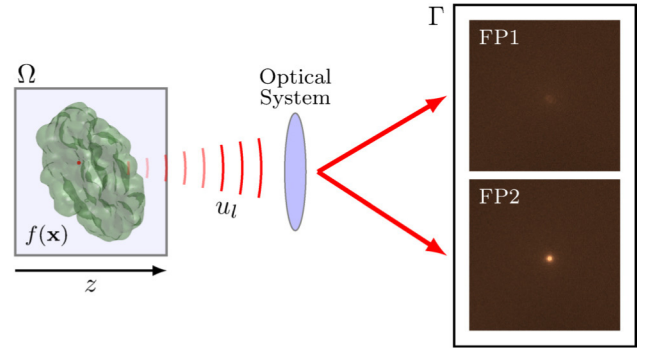


Fig. 1. Biplane single-molecule localization microscopy. A fluorophore emits fluorescent light which scatters through the sample. Then, an optical system records the intensity of the total field at two different focal planes.

Algorithm 1 Joint-Optimization Framework

Require: $\mathbf{f}^0 \in \mathbb{R}_{\geq 0}^N$, $[\mathbf{x}_1^0 \dots \mathbf{x}_L^0] \in \Omega^L$, $\mathbf{a}^0 \in \mathbb{R}_{> 0}^L$

```

1:  $t = 0$ 
2: while (Not converged) do
3:   Select a subset  $\mathcal{L} \subset \{1, \dots, L\}$ 
    $\triangleright$  Update amplitudes and positions
4:   for  $l \in \mathcal{L}$  do
5:      $(a_l^{t+1}, \mathbf{x}_l^{t+1}) = \text{Refine}(\mathcal{J}_l(\mathbf{f}^t, \cdot, \cdot), a_l^t, \mathbf{x}_l^t)$ 
6:   end for
    $\triangleright$  Update the scattering potential:
7:    $\mathbf{f}^{t+1} = \text{aFBS}(\sum_{l \in \mathcal{L}} \mathcal{J}_l(\cdot, \mathbf{x}_l^{t+1}, a_l^{t+1}); \mathbf{f}^t)$ 
8:    $t \leftarrow t + 1$ 
9: end while

```

Return: $\mathbf{f}^t, \mathbf{X}^t, \mathbf{a}^t$

the sample and produces a field $u_l : \mathbb{R}^3 \rightarrow \mathbb{C}$ that satisfies the Lippmann–Schwinger equation

$$u_l(\mathbf{x}) = u_{\text{in}}(\mathbf{x}; \mathbf{x}_l, a_l) + \int_{\Omega} g(\mathbf{x} - \mathbf{z}) f(\mathbf{z}) u_l(\mathbf{z}) d\mathbf{z}, \quad (2)$$

where $f(\mathbf{x}) = k_b^2 \left(\frac{\eta(\mathbf{x})^2}{\eta_b^2} - 1 \right)$ is the scattering potential and $g : \mathbb{R}^3 \rightarrow \mathbb{C}$ is the Green function that corresponds to the centered spherical wave $u_{\text{in}}(\mathbf{x}; \mathbf{0}, 1)$ [16]. The intensity of the field u_l at the camera plane Γ is then recorded by an optical system to form the l th SMLM frame $\mathbf{y}_l \in \mathbb{R}^M$. Formally, we have, $\forall l \in \{1, \dots, L\}$, that

$$\mathbf{y}_l = \text{Pois} \left(|P u_l|_{\Gamma}|^2 + \mathbf{b}_l \right), \quad (3)$$

where Pois denotes Poisson’s distribution (shot noise), $u_l|_{\Gamma}$ denotes the restriction of u_l to Γ , and $\mathbf{b}_l \in \mathbb{R}^M$ is a background signal that can originate from autofluorescence or spurious out-of-focus fluorophore emissions. Finally, $P : \mathbb{C}^2 \rightarrow \mathbb{R}^M$ is a linear operator that models both the effect of the optical system (i.e., pointwise multiplication with the pupil function in the Fourier domain) and the sampling on the M camera pixels (see Fig. 1).

2.2. Discrete forward model

Let us rasterize Ω into N voxels of length h . Following [17–19], we define the discrete forward model by

$$\mathbf{H} : \mathbb{R}_{\geq 0}^N \times \Omega \times \mathbb{R}_{> 0} \rightarrow \mathbb{R}^M$$

$$(\mathbf{f}, \mathbf{x}_l, a_l) \mapsto \mathbf{B} \left| \mathbf{P} [\mathbf{A}(\mathbf{f}), \mathbf{I}_M] \mathbf{s}_{\text{in}}(\mathbf{x}_l, a_l) \right|^2 \quad (4)$$

with

$$\mathbf{A}(\mathbf{f}) = \tilde{\mathbf{G}} \text{diag}(\mathbf{f}) (\mathbf{I}_N - \mathbf{G} \text{diag}(\mathbf{f}))^{-1}, \quad (5)$$

$$\mathbf{s}_{\text{in}}(\mathbf{x}_l, a_l) = [(\mathbf{u}_{\text{in},l}^{\Omega})^T, (\mathbf{u}_{\text{in},l}^{\Gamma})^T]^T. \quad (6)$$

Here, $\mathbf{f} \in \mathbb{R}^N$ is a sampled version of f within Ω . The vectors $\mathbf{u}_{\text{in},l}^{\Omega} \in \mathbb{C}^N$ and $\mathbf{u}_{\text{in},l}^{\Gamma} \in \mathbb{C}^M$ are the sampled versions of $u_{\text{in}}(\cdot; \mathbf{x}_l, a_l)$ within Ω and Γ , respectively. We denote by $\{\mathbf{x}_n^{\Omega}\}_{n=1}^N$ and $\{\mathbf{x}_m^{\Gamma}\}_{m=1}^M$ the sampling points within Ω and Γ . The matrix $\mathbf{G} \in \mathbb{C}^{N \times N}$ encodes the convolution with the Green function in (2). Similarly, $\tilde{\mathbf{G}} \in \mathbb{C}^{M \times N}$ is a matrix that, given the total field within Ω , gives the scattered field at the measurement plane Γ . Next, $\mathbf{P} \in \mathbb{C}^{M \times M}$ is the discrete version of P and $|\cdot|^2$ denotes the pointwise-squared magnitude. A full description of \mathbf{G} , $\tilde{\mathbf{G}}$, and \mathbf{P} is provided in [19]. Finally, the matrix $\mathbf{B} \in \mathbb{R}^{M \times M}$ encodes a convolution with a Gaussian filter of length $\sigma_b = 0.7h$. It accounts for the mismatch between our physical model derived from the scalar diffraction theory and the vectorial nature of light [20,21].

In this work, we adopt a biplane configuration [22] that involves two pupil functions with separate focal planes. To keep the notation simple, we shall use a single matrix \mathbf{P} to represent the effect of the two pupil functions (i.e., two focal planes). Given the discrete forward model (4), the image formation model (3) writes as, $\forall l \in \{1, \dots, L\}$,

$$\mathbf{y}_l = \text{Pois}(\mathbf{H}(\mathbf{f}, \mathbf{x}_l, a_l) + \mathbf{b}_l). \quad (7)$$

Remark 1. Although we consider a biplane modality in our experiments, the proposed joint optimization framework (Section 3) can be deployed with any number of focal planes. In this proof-of-concept work, we considered two focal planes because (i) it corresponds to a standard SMLM modality (ii) it helps to compensate for the lack of phase measurements.

3. Joint recovery of the molecule localization and refractive index

3.1. Joint-optimization framework

Our goal is to jointly recover the distribution of the refractive index and the localization of fluorescent molecules. To that end, we propose to solve the minimization problem

$$(\mathbf{f}_*, \mathbf{X}_*, \mathbf{a}_*) \in \arg \min_{\substack{\mathbf{f} \in \mathbb{R}_{\geq 0}^N \\ \mathbf{X} \in \Omega^L, \mathbf{a} \in \mathbb{R}_{> 0}^L}} \sum_{l=1}^L J_l(\mathbf{f}, \mathbf{x}_l, a_l) + \tau \mathcal{R}(\mathbf{f}), \quad (8)$$

where, for all $\mathbf{f} \in \mathbb{R}_{\geq 0}^N$, $\mathbf{x} \in \Omega$, and $a > 0$,

$$J_l(\mathbf{f}, \mathbf{x}, a) = D_{\text{KL}}(\mathbf{H}(\mathbf{f}, \mathbf{x}, a) + \mathbf{b}_l; \mathbf{y}_l). \quad (9)$$

The matrix $\mathbf{X} = [\mathbf{x}_1 \dots \mathbf{x}_L] \in \Omega^L$ and the vector $\mathbf{a} = (a_1, \dots, a_L) \in \mathbb{R}_{> 0}^L$ are the concatenation of positions and amplitudes of the fluorophores, respectively. The functional $\mathcal{R} : \mathbb{R}^N \rightarrow \mathbb{R}_{\geq 0}$ is a regularization term that introduces prior knowledge on the RI distribution, and $\tau > 0$ is a tradeoff parameter. In this work, we use the total-variation (TV) regularization [23], although alternatives such as the Hessian-Schatten norm [24] or learnt regularizers [25–28] can be easily plugged into our framework. The data-fidelity term D_{KL} is the Kullback–Leibler divergence [29] defined as, $\forall (\mathbf{z}, \mathbf{y}) \in \mathbb{R}_{\geq 0}^M \times \mathbb{R}_{\geq 0}^M$,

$$D_{\text{KL}}(\mathbf{z}; \mathbf{y}) = \mathbf{z}^T \mathbf{1}_M - \mathbf{y} \odot \log(\mathbf{z} + \beta), \quad (10)$$

where $\beta > 0$ is a stabilizing parameter. Note that the Kullback–Leibler divergence corresponds to the Poisson negative log-likelihood up to some constant term.

To optimize (8), we alternate between an update of the refractive index and an update of the amplitudes and positions of the fluorophores (Algorithm 1), inspired by the self-calibrating reconstruction techniques developed for other modalities [30,31]. Updates are performed on a subset of molecules (Line 3) in a stochastic fashion. In Algorithm 1, aFBS ($\sum_{l \in \mathcal{L}} J_l(\cdot, \mathbf{x}_l^{t+1}, a_l^{t+1}; \mathbf{f}^t)$) refers to the minimization

Algorithm 2 Refinement procedure for the l th molecule

Require: $\mathbf{x}_l^0 \in \Omega$, $a_l^0 > 0$, $T_{\text{mol}} \in \mathbb{N}$

1: $t = 0$

2: **while** (Not converged or $t < T_{\text{mol}}$) **do**

3: $a_l^{t+1} = \text{NewtonUpdate}(J_l(\mathbf{f}, \mathbf{x}_l^t, \cdot); a_l^t)$

4: $\mathbf{x}_l^{t+1} = \text{GradientUpdate}(J_l(\mathbf{f}, \cdot, a_l^{t+1}); \mathbf{x}_l^t)$

5: $t \leftarrow t + 1$

6: **end while**

Return: \mathbf{x}_l^t, a_l^t

of $\sum_{l \in \mathcal{L}} J_l(\cdot, \mathbf{x}_l^{t+1}, a_l^{t+1})$ with the algorithm aFBS initialized with \mathbf{f}^t . We use the same notation for the refinement step at Line 5. Details on the algorithms deployed for each sub-problem are provided in Sections 3.2 and 3.3. We implemented the method within the GlobalBioIm framework [32].

3.2. Update of molecule amplitudes and positions

For the refinement procedure in Line 5 of Algorithm 1, we again adopt an alternating scheme between an update of the amplitude and the position, as summarized in Algorithm 2. In the Sections 3.2.1 and 3.2.2, we describe the Newton and gradient update steps used to refine the amplitude and position, respectively.

3.2.1. Amplitudes

Let $\mathbf{f} \in \mathbb{R}_{\geq 0}^N$ and $\mathbf{X} \in \Omega^L$ be fixed. First of all, one can see from (4) that, for $a_l > 0$,

$$\mathbf{H}(\mathbf{f}, \mathbf{x}_l, a_l) = a_l^2 \mathbf{H}(\mathbf{f}, \mathbf{x}_l, 1), \quad (11)$$

which is very helpful to reduce the computational cost of our joint-optimization procedure. Indeed, denoting $\mathbf{v}_l = \mathbf{H}(\mathbf{f}, \mathbf{x}_l, 1)$, we have that

$$J_l(\mathbf{f}, \mathbf{x}_l, a_l) = D_{\text{KL}}(a_l^2 \mathbf{v}_l + \mathbf{b}_l; \mathbf{y}_l) \quad (12)$$

$$= (a_l^2 \mathbf{v}_l + \mathbf{b}_l)^T \mathbf{1}_M - \mathbf{y}_l \odot \log(a_l^2 \mathbf{v}_l + \mathbf{b}_l + \beta). \quad (13)$$

The function J_l is twice differentiable with respect to a . Its first derivative is given by

$$\partial_a J_l(\mathbf{f}, \mathbf{x}_l, a_l) = 2a_l \sum_{m=1}^M v_{lm} \left(1 - \frac{y_{lm}}{a_l^2 v_{lm} + b_{lm} + \beta} \right). \quad (14)$$

Its second derivative reads as

$$\begin{aligned} \partial_a^2 J_l(\mathbf{f}, \mathbf{x}_l, a_l) &= 2 \sum_{m=1}^M v_{lm} \left(1 - \frac{y_{lm}}{a_l^2 v_{lm} + b_{lm} + \beta} \right) \\ &\quad + \sum_{m=1}^M \frac{(2a_l v_{lm})^2 y_{lm}}{(a_l^2 v_{lm} + b_{lm} + \beta)^2}. \end{aligned} \quad (15)$$

As such, we can perform a Newton update on a_l as

$$a_l^{t+1} = a_l^t - s \frac{\partial_a J_l(\mathbf{f}, \mathbf{x}_l, a_l^t)}{\partial_a^2 J_l(\mathbf{f}, \mathbf{x}_l, a_l^t)}, \quad (16)$$

where s is the length of a step computed via line-search so as to satisfy Wolfe's conditions [33].

3.2.2. Positions

Let $\mathbf{f} \in \mathbb{R}_{\geq 0}^N$ and $\mathbf{a} \in \mathbb{R}_{> 0}^L$ be fixed. We want to perform a gradient update on the position \mathbf{x}_l of the l th molecule. However, one can see that the spherical wave in (1) is not differentiable whenever $\mathbf{x} = \mathbf{x}_l$. Consequently, we prefer to consider the smoothed version of the spherical wave

$$u_{\text{in}}^{\text{smth}}(\mathbf{x}; \mathbf{x}_l, a_l) = a_l \frac{\exp(jk_b \|\mathbf{x} - \mathbf{x}_l\|_{2,\epsilon})}{4\pi \|\mathbf{x} - \mathbf{x}_l\|_{2,\epsilon}}, \quad (17)$$

Algorithm 3 aFBS**Require:** $\mathbf{f}^0 \in \mathbb{R}_{\geq 0}^N$, $T_{\text{RI}} \in \mathbb{N}$, $\gamma > 0$, $\alpha \in [0, 1]$

```

1:  $t = 0$ ,  $\mathbf{w}^0 = \mathbf{f}^0$ ,  $v^0 = 1$ 
2: while (Not converged or  $t < T_{\text{RI}}$ ) do
3:    $\mathbf{g} = \sum_{l \in \mathcal{L}} \nabla J_l(\cdot, \mathbf{x}_l, a_l)(\mathbf{w}^t)$ 
4:    $\mathbf{f}^{t+1} = \text{prox}_{\gamma \tau \mathcal{R}}(\mathbf{w}^t - \gamma \mathbf{g})$ 
5:    $v^{t+1} = \frac{1 + \sqrt{1 + 4(v^t)^2}}{2}$ 
6:    $\mathbf{w}^{t+1} = \mathbf{f}^t + \alpha \frac{v^t - 1}{v^{t+1}}(\mathbf{f}^t - \mathbf{f}^{t+1})$ 
7:    $t \leftarrow t + 1$ 
8: end while

```

Return: \mathbf{f}^t

where $\|\cdot\|_{2,\epsilon} = \sqrt{\|\cdot\|_2^2 + \epsilon}$ with $0 < \epsilon \ll 1$. Then, the gradient of J_l with respect to \mathbf{x}_l , evaluated at \mathbf{x}_l , is given by

$$\nabla_{\mathbf{x}_l} J_l(\mathbf{f}, \mathbf{x}_l, a_l) = 2\mathbf{J}_{s_{\text{in},l}}^H [\mathbf{A}(\mathbf{f}), \mathbf{I}_M]^H \mathbf{P}^H \mathbf{P} [\mathbf{A}(\mathbf{f}), \mathbf{I}_M] s_{\text{in},l} \odot \mathbf{B}^T \nabla_{\mathbf{z}} D_{\text{KL}}(\mathbf{H}(\mathbf{f}, \mathbf{x}_l, a_l) + \mathbf{b}_l), \quad (18)$$

where $s_{\text{in},l} = s_{\text{in}}(\mathbf{x}_l, a_l) \in \mathbb{C}^{N+M}$. The gradient of D_{KL} in (10) with respect to the first variable \mathbf{z} is given by

$$\nabla_{\mathbf{z}} D_{\text{KL}}(\mathbf{z}; \mathbf{y}) = \mathbf{I}_M - \mathbf{y}_l \odot (\mathbf{z} + \beta). \quad (19)$$

Finally, it remains to provide the expression of the Hermitian transpose of the Jacobian matrix of $s_{\text{in}}(\cdot, a_l)$, evaluated at \mathbf{x}_l , which we denote $\mathbf{J}_{s_{\text{in},l}}^H \in \mathbb{C}^{3 \times (N+M)}$. Its q th column is given by

$$[\mathbf{J}_{s_{\text{in},l}}^H]_q = [\mathbf{s}_{\text{in},l}]_q^* \left(jk_b + \frac{1}{\|\mathbf{r}_q - \mathbf{x}_l\|_{2,\epsilon}} \right) \frac{(\mathbf{r}_q - \mathbf{x}_l)}{\|\mathbf{r}_q - \mathbf{x}_l\|_{2,\epsilon}}. \quad (20)$$

Let us emphasize that $\mathbf{r}_q = \mathbf{x}_q^\Omega$ (Ω sampling points) for $q \leq N$ and $\mathbf{r}_q = \mathbf{x}_{q-N}^\Gamma$ (Γ sampling points) for $N < q \leq N + M$. Equipped with this closed-form gradient, we can deploy a projected-gradient update on \mathbf{x}_l as

$$\mathbf{x}_l^{t+1} = \mathcal{P}_\Omega(\mathbf{x}_l^t - s \nabla_{\mathbf{x}_l} J_l(\mathbf{f}, \mathbf{x}_l^t, a_l)), \quad (21)$$

where s is a step-size computed via a backtracking line-search [34]. The projector $\mathcal{P}_\Omega : \mathbb{R}^3 \rightarrow \Omega$ constrains the fluorophore positions to remain in Ω .

3.3. Update of the refractive index

When the positions $\mathbf{X} \in \Omega^L$ and amplitudes $\mathbf{a} \in \mathbb{R}_{>0}^L$ are fixed, the RI update consists in solving

$$\mathbf{f}^* \in \arg \min_{\mathbf{f} \in \mathbb{R}_{\geq 0}^N} \sum_{l=1}^L J_l(\mathbf{f}, \mathbf{x}_l, a_l) + \tau \mathcal{R}(\mathbf{f}). \quad (22)$$

It corresponds to an inverse-scattering problem from intensity measurements [35,36]. To solve (22), we deploy a relaxed variant [37] of the accelerated forward-backward splitting (aFBS) algorithm [38,39] (Algorithm 3). It requires the computation of two quantities.

1. The gradient of $J_l(\cdot, \mathbf{x}_l, a_l)$ which involves the Jacobian of $\mathbf{A}(\mathbf{f})$ in (4) whose expression is provided in [18].
2. The proximal operator of \mathcal{R} which, for TV, can be efficiently evaluated by using the fast gradient-projection algorithm [40].

3.4. Initialization strategies

3.4.1. Initialization of the refractive index

In phaseless diffraction tomography, the light-field refocusing method is a standard tool to obtain an initial guess of the RI distribution [35,41]. However, this initialization requires coherent light

sources with known geometry, which prevents its use on SMLM data. We therefore adopt an alternative approach that comprises two steps. We first replicate the widefield image (sum of the SMLM stack) along the axial direction and then blur the obtained volume with a Gaussian filter. The rationale behind this choice is that we can only expect to recover the RI where fluorophore emissions have propagated, that is, at the vicinity of fluorescent molecules. We then define \mathbf{f}^0 as a scaled version of this filtered volume so that its values belong to an admissible range of RI (see Fig. 3).

3.4.2. Single-molecule localization

Any SMLM localization software can be used to compute the initial positions $\{\mathbf{x}_l^0\}_{l=1}^L$. However, we found that existing software packages for a biplane modality were not performing well on our simulated dataset. We believe that this is due to the high thickness of the sample together with the small number of acquisitions.

Therefore, we adopted a simple yet efficient method. We localize the position of the l th fluorophore based on cross-correlations between the measurements \mathbf{y}_l and a set $\{\mathbf{k}_p\}_{p=1}^P$ of PSF models in \mathbb{R}^M . We define them as the output of the forward model with no scatterer, like in

$$\mathbf{k}_p = \mathbf{H}(\mathbf{0}_N, \mathbf{x}_p^{\text{psf}}, 1), \quad (23)$$

where the positions $\mathbf{x}_p^{\text{psf}} = (0, 0, p\Delta z)$ for $p = \{-P, \dots, P\}$ vary along the axial direction. We then initialize

$$\mathbf{x}_l^0 = (\hat{m}h, \hat{n}h, \hat{p}\Delta z) \quad (24)$$

where

$$(\hat{m}, \hat{n}, \hat{p}) = \arg \max_{m, n, p} [\mathbf{y}_l \star \mathbf{k}_p^V]_{m,n}, \quad (25)$$

with \star the 2D discrete convolution and $(\cdot)^V$ the reflection operator. Once localized, we initialize the amplitude as

$$a_l^0 = \left(\|\mathbf{M}_{\mathbf{x}_l^0}(\mathbf{y}_l - \hat{\mathbf{b}}_l)\|_1 / \|\mathbf{k}_{\hat{p}}\|_1 \right)^{\frac{1}{2}}, \quad (26)$$

where $\mathbf{M}_{\mathbf{x}_l^0} \in \mathbb{R}^{R \times M}$ crops a region-of-interest centered at \mathbf{x}_l^0 and $\hat{\mathbf{b}}_l$ denotes the estimated background (see Section 3.4.3).

3.4.3. Background estimation

To estimate $\{\mathbf{b}_l\}_{l=1}^L$, we apply a simple algorithm suitable for a background that slowly varies in space and time. In SMLM, this is a common assumption [42]. Our procedure proceeds in two steps.

1. For each measurement \mathbf{y}_l , we mask an area around the estimated position \mathbf{x}_l and inpaint it using the function `regionfill` of Matlab¹ to obtain $\tilde{\mathbf{y}}_l$.
2. We apply a spatio-temporal (3D) median filter along the stack of masked and inpainted measurements $\tilde{\mathbf{Y}} = [\tilde{\mathbf{y}}_1 \dots \tilde{\mathbf{y}}_L]$ to take advantage of the spatio-temporal smoothness of the background.

4. Numerical experiments

4.1. Simulation setting

We created an RI volume immersed in water ($\eta_b = 1.339$), fully included in the region Ω of size $(7.2 \times 7.2 \times 3.2) \mu\text{m}^3$ (Fig. 2). This sample presents small features with RI values that are lower or higher than their surroundings. Then, we populated this sample with fluorophores randomly placed on a structure that is composed of an outer membrane as well as inner compartments. The smallest distance between two fluorophores is 20 nm. We simulated $L = 1000$ SMLM acquisitions with a biplane modality, each corresponding to the activation of a single fluorophore. The two focal planes were set at ± 300 nm. The

¹ Matlab's command `regionfill` performs a smooth interpolation inward from the pixel values that are on the outer boundary of the mask.

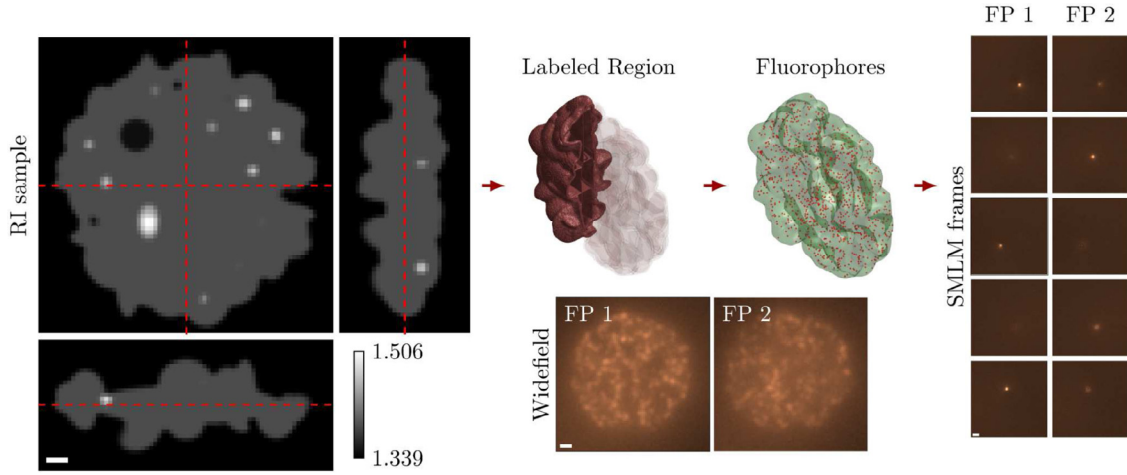


Fig. 2. Simulation setup. The RI map, immersed in water ($n_b = 1.339$), is depicted on the left orthoviews. The sample is populated with fluorescent molecules that belong to the labeled region. They sequentially emit a spherical wave which is then propagated through the sample using the Lippmann-Schwinger model. Two focal planes (with pupil functions) are acquired. The widefield images are generated by summing all SMLM frames. The fluorescence images were saturated for visualization purpose. We display the labeled region with partial transparency so as to make the inner compartments visible. Scale bars: 500 nm.

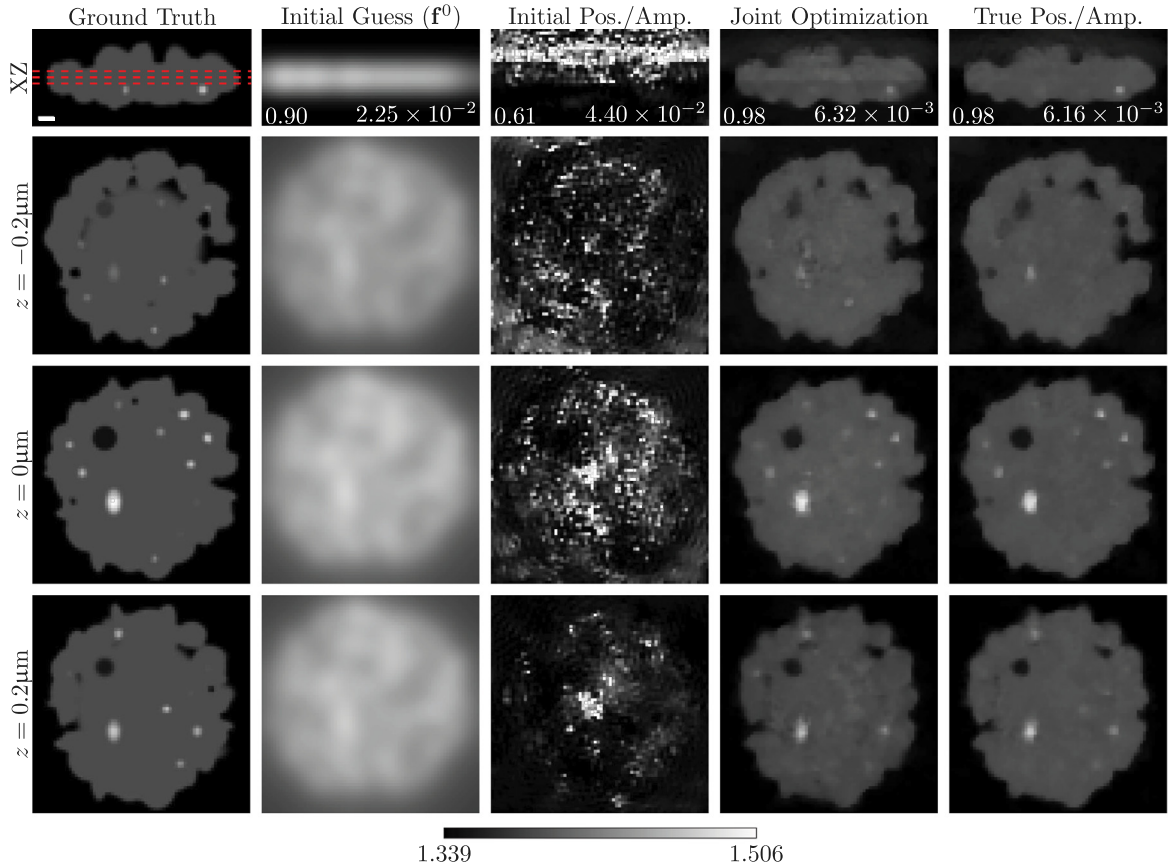


Fig. 3. Reconstructions of the RI volume. From left to right: Ground truth, initial guess, reconstruction with positions and amplitudes fixed to their initial values (see Section 3.4.2), reconstruction with the proposed joint-optimization framework, and reconstruction with positions and amplitudes fixed to their true values (gold-standard). The SSIM and relative errors are displayed in the first row at the left and right corners, respectively, of each corresponding reconstruction. Scale bar: 500 nm.

amplitude a_i of each fluorophore emission was drawn from a Poisson distribution with mean $A = 1000$ and the wavelength of the emitted light is set at $\lambda = 647$ nm. In addition, we simulated a pupil function for each focal plane with $\text{NA} = 1.45$ and 25 Zernike coefficients. Their values were drawn from the uniform distribution $U(-0.5, 0.5)$, except that the three first coefficients were set to 0 and that the fourth coefficient was drawn from $U(-0.1, 0.1)$ to better match the PSFs observed in real SMLM acquisitions. The background signals b_i for

$l \in \{1, 100, 200, \dots, 1000\}$ were simulated by convolving a Gaussian kernel with a random image generated from a uniform distribution. We then scaled the obtained images so that their pixel values belong to the range $[350, 450]$. Backgrounds for intermediate frames were then obtained through interpolation. We set a large width for the Gaussian kernel so as to obtain a slowly varying background in both space and time. Finally, to control the noise, we scaled the noiseless measurements with a factor $r \in (0, 1]$ before applying the Poisson noise so that

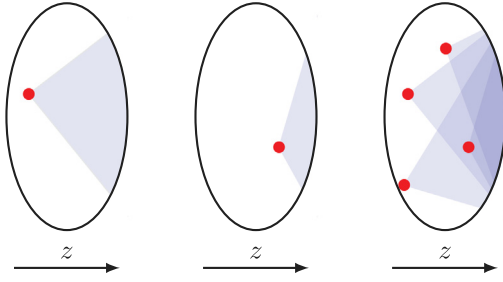


Fig. 4. Observable region of the sample. Illustration of the region of the sample that is “illuminated” by a fluorophore far from (left) and close to (middle) the detection system. The right scheme illustrates the fact that SMLM data carry more information about RI regions that are close to the detection system (positive z).

(4) writes as, $\forall l \in \{1, \dots, L\}$,

$$\mathbf{y}_l = \text{Pois}(r(\mathbf{H}(\mathbf{f}, \mathbf{x}_l, a_l) + \mathbf{b}_l)). \quad (27)$$

By doing so, r can be interpreted as the product between the excitation photon flux and the integration time. A small r yields a higher level of noise, which increases the difficulty of the localization of molecules and the RI reconstruction.

We compare our joint-optimization framework with two baselines. They consist on the sole RI reconstruction with i) perfectly characterized molecules (i.e., true amplitudes and positions) or ii) the initial estimation of the amplitudes and positions obtained as described in Section 3.4.2. By doing so, we somehow obtain the worst-case and best-case scenarios. For each case, we obtained the best reconstruction by performing a grid search on the regularization parameter τ .

For our joint-optimization framework, we set the parameters $T_{\text{mol}} = 4$, $T_{\text{RI}} = 1$, and $\alpha = 0.85$. In our implementation, \mathbf{w}^0 and \mathbf{v}^0 in Line 1 of Algorithm 3 are initialized from the previous call. We ran our optimization on a PowerEdge c4140 equipped with Intel Xeon Gold 6240 CPUs (2.60 GHz) and a GPU NVIDIA Tesla V100 SXM3 (32 GB). An iteration of Algorithm 1 took 20 s on average. We used up to 2000 iterations, which corresponds to about 10 h of computation.

4.2. Metrics and visualization

To assess the quality of the reconstructed RI volume, we compute the relative error as well as the structural similarity index measure (SSIM) [43] with respect to the ground-truth. To assess the accuracy of the localization of the molecules, we compute the root-mean-square error (RMSE) with respect to the true positions. Note that we do not report detection metrics such as true/false detections as they are not really relevant in our setting where we consider only frames containing one molecule. Finally, given a list of molecule positions, we generate a 3D image through the Gaussian rendering technique [6]. To that end, we represent the fluorophore positions as a sum of shifted Dirac

$$s(\mathbf{x}) = \sum_{l=1}^L \delta(\mathbf{x} - \mathbf{x}_l). \quad (28)$$

Gaussian rendering then consists in convolving s with an isotropic Gaussian kernel and sample the result on a grid. Here, we set the standard deviation of the Gaussian kernel to 10 nm and the grid step to $h/10 = 10$ nm.

4.3. Results

We first fix the noise level to $r = 1$ in (27).

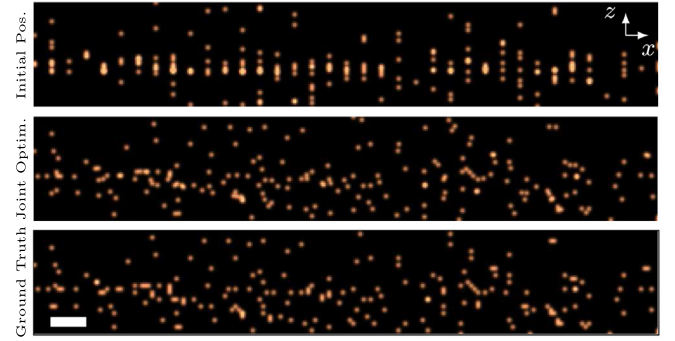


Fig. 5. Rendering of localized molecules (Y-projection). Region-of-interest of the projection along Y of the rendered fluorescent volume. From top to bottom: Initial positions, positions refined with the joint-optimization framework, ground-truth. Field-of-view (XZ): $(3600 \times 600) \text{ nm}^2$. The images were saturated for visualization purpose. Scale bar: 200 nm.

4.3.1. Reconstructed refractive index

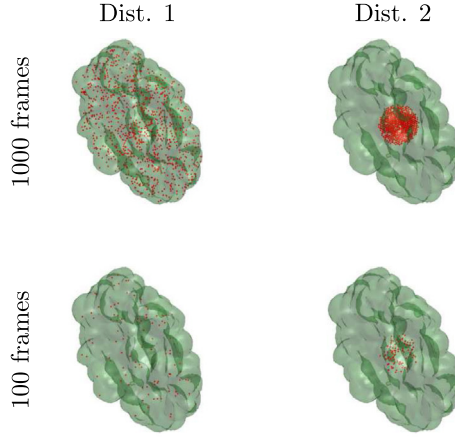
We display the RI volumes in Fig. 3 and report there the relative errors and SSIM. When the positions and amplitudes of the molecules are perfectly known, we recover most of the details of the ground-truth. This is in line with our previous work [13]. On the contrary, the reconstruction obtained with the initial positions and amplitudes is unsuccessful. This highlights the importance of refining molecule positions and amplitudes jointly with RI reconstruction. We effectively see that our joint-optimization framework is able to recover an RI volume that is visually similar to the best-case scenario. The metrics confirm the visual assessment. Yet, one can observe some high frequency artifacts (ringing) on the reconstruction obtained with the joint optimization framework (plane $z = -0.2 \mu\text{m}$). They are due to few badly refined molecule positions (outliers in Fig. 8) that lead to a mismatch in the model. Finally, it should be noted that we could expect that the quality of the reconstruction varies with the axial position z . The reason is that an SMLM frame (from the activation of one molecule) carries information about the part of sample that lies between the activated molecule and the optical system (see Fig. 4). As such, there are more SMLM frames that carry information about z -planes with positive z than frames that carry information about z -planes with negative z . Moreover, waves produced by fluorophores with negative z -positions propagate through a larger layer of the sample, inducing more scattering. These facts make that i) fluorophores with negative z -positions are harder to localize, and ii) z -planes of RI with negative z are harder to reconstruct.

4.3.2. Molecule localization

It is noteworthy to recall that the primary objective of SMLM is to localize the fluorescent molecules with nanometric precision. It follows that another benefit of our joint-optimization framework is an improvement of this localization. Indeed, our model accounts for sample-induced distortions that usually compromises the accurate localization of molecules [9].

We report in Table 1 the RMSE of the initial and refined positions, as well as the RMSE of the initial and refined amplitudes. In addition, we provide the RMSE of the refined positions and amplitudes when the RI map is fixed to the initial guess \mathbf{f}^0 or the ground-truth (best-case scenario). There is a gain of 89 nm in the 3D RMSE for our joint-optimization framework. One sees that the lateral and axial RMSE are improved by 54 nm and 76 nm, respectively. Not only does our joint-optimization framework successfully recover the RI volume, but it also improves significantly the localization of the molecules. The proposed joint-optimization framework performs better than the refinement of the positions and amplitudes with the RI map fixed to \mathbf{f}^0 . Moreover, it performs similarly to the refinement with the RI map fixed to the

A: Distribution of fluorophores



B: RI reconstruction

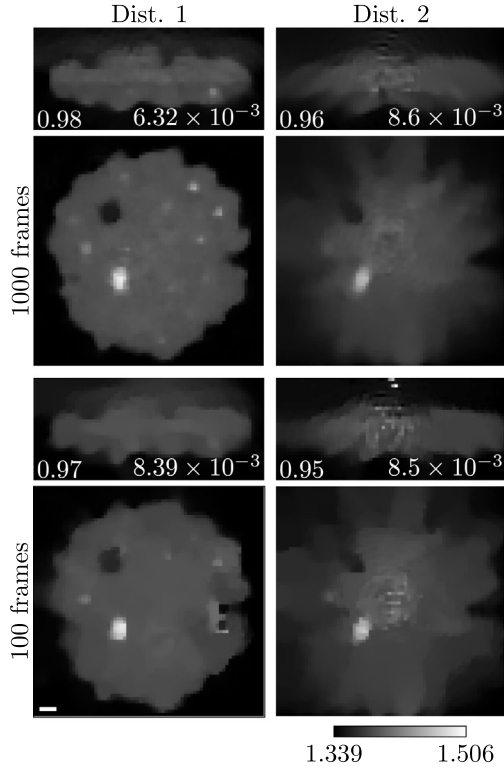


Fig. 6. Reconstructions of the RI volume with different fluorophore distributions. A: The four considered fluorophore distributions. B: Reconstructed RI maps. The SSIM and relative errors are displayed in the XZ view at the left and right corners of each reconstruction, respectively. The signal-to-noise ratio is displayed at the bottom-left corner for each noise level. Scale bar: 500 nm.

ground-truth. Those observations confirm that the joint-optimization framework is necessary to improve the localization and can even reach similar performance to the best-case scenario.

In Fig. 5, we display a Y-projection of the fluorescent volume rendered from the molecule positions, where one can visually appreciate the gain in accuracy. The estimation of the amplitudes is improved as well. This can help to better estimate the uncertainty of localization [44,45].

Table 1

RMSE for the estimated positions and amplitudes. First row: Initial positions and amplitudes from our standard single-molecule localization. Second row: Positions and amplitudes from our joint-optimization framework. Third and fourth rows: Positions and amplitudes refined with the RI map fixed to the initial guess \mathbf{f}^0 and the ground-truth (GT), respectively. Amp.: Amplitude. Lat.: Lateral. Ax.: Axial.

	3D [nm]	Lat. [nm]	Ax. [nm]	Amp.
Initial	163	69	148	109
Joint	74	15	72	76
with \mathbf{f}^0	142	38	136	194
with \mathbf{f}_{GT}	72	18	70	76

Table 2

RMSE of the estimated positions and amplitudes for the four distributions of fluorophores depicted in Fig. 6 (Panel A). Amp.: Amplitude. Lat.: Lateral. Ax.: Axial. Dist.: Distribution.

	#Fluo	3D [nm]	Lat. [nm]	Ax. [nm]	Amp.
Dist. 1	1000	74	15	72	76
	100	80	13	79	76
Dist. 2	1000	85	3	85	77
	100	82	3	82	55

4.3.3. Influence of the distribution of fluorophores

From the phenomenon illustrated in Fig. 4, one can expect that the quality of the reconstructed RI map is closely related to the spatial distribution of the fluorescent probes. In this section, we investigate this question by comparing the reconstructions obtained with the four fluorophore distributions illustrated in Fig. 6 (Panel A). These include the rather homogeneous distribution depicted in Fig. 2 and a more concentrated distribution, both with two different numbers of molecules (*i.e.*, numbers of frames).

As expected, the reconstructed RI map is significantly degraded when the distribution of fluorophores is more concentrated (Fig. 6B, right column). Indeed, the emitted light has mainly propagated through a restricted area of the sample, limiting the information on the RI map carried by the measurements. On the contrary, the quality of the reconstructed RI map seems less sensitive to the number of fluorophores. Although some details are lost, the RI maps reconstructed with 100 frames remain qualitatively similar to their counterparts reconstructed from 1000 frames (Fig. 6B).

Finally, we display in Table 2 the RMSE obtained after the joint optimization. Interestingly, the refinement of the positions and amplitudes of the molecules remains stable when reducing the number of frames. For the concentrated distribution, the axial RMSE is slightly degraded and, on the contrary, the lateral RMSE is drastically reduced, which might be due to the concentration of the distribution.

4.3.4. Robustness to noise

Next, we are interested in the robustness of our framework to the measurement noise. To that end we vary the parameter r in (27) from 0.1 to 1. Some examples of obtained measurements are shown in Fig. 7 (last row), where one can observe that the noise is stronger when r is smaller. The RI reconstructions for each noise level are displayed in Fig. 7. Although the quality of reconstruction degrades when the noise increases, the shape and the most prominent features are recognizable even for $r = 0.1$. This suggests that our method is quite robust to noise.

The box plots of the localization errors are displayed in Fig. 8. For each noise level, we show the box plot for the initial and refined positions to illustrate the improvement. We again observe a certain robustness to noise, even for the case $r = 0.1$ where the amplitudes were badly initialized. It is noteworthy to mention the presence of outliers in the displayed box plots even for $r = 1$. For some molecules, we observed that the joint-optimization could not refine the positions and amplitudes well. In few cases, the estimates did even worsen. Fortunately, the number of such failures is limited (*e.g.*, 60 over 1000 molecules for $r = 0.1$).

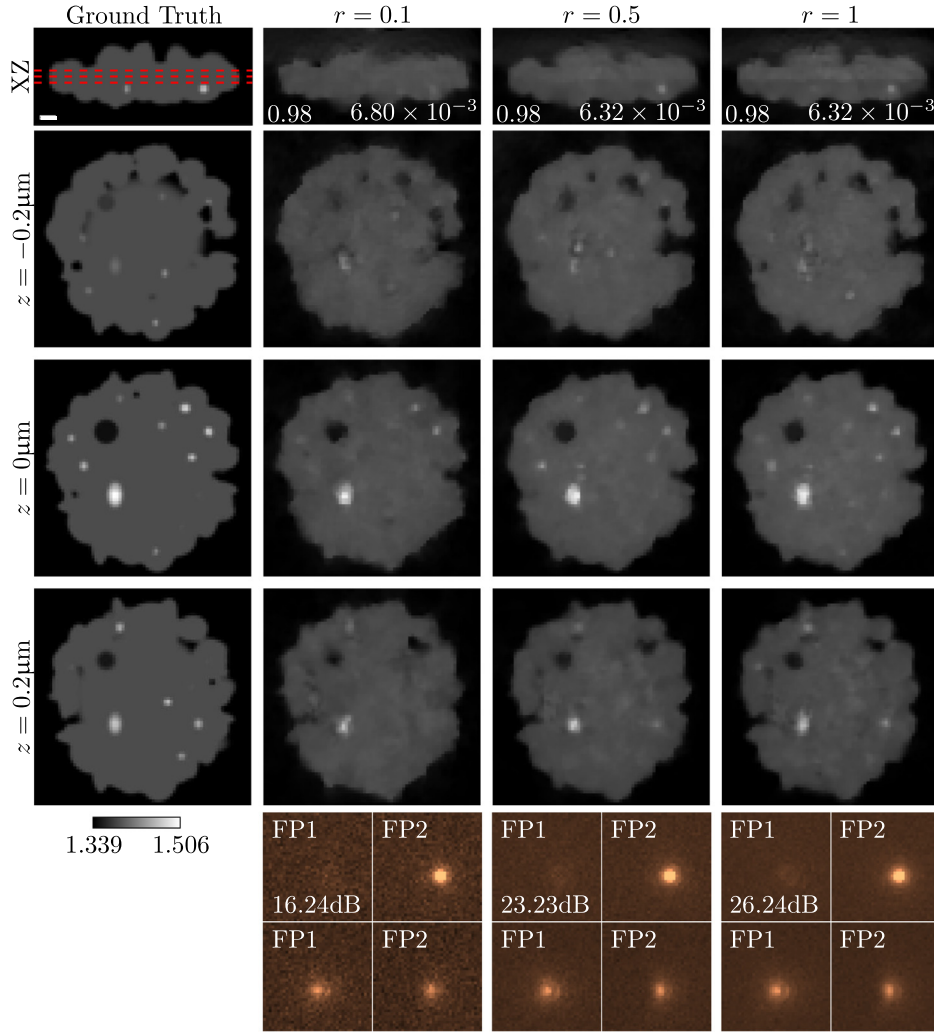


Fig. 7. Reconstructions of the RI volume with different noise levels. From left to right: Ground truth, reconstruction with the proposed joint optimization framework for $r = 0.1, 0.5$, and 1. The SSIM and relative errors are displayed in the first row at the left and right corners of each reconstruction, respectively. The last row contains two examples of SMLM acquisition (ROI) for two different molecules at axial positions $z = 440 \text{ nm}$ (top) and $z = 0 \text{ nm}$ (bottom). The signal-to-noise ratio is displayed at the bottom-left corner for each noise level. Scale bar: 500 nm.

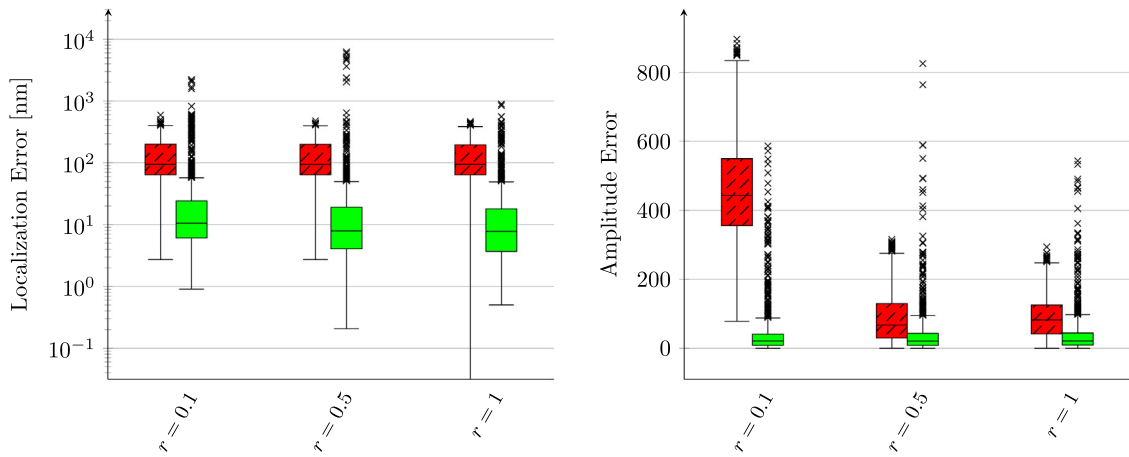


Fig. 8. Box plots of the localization (left) and amplitude (right) error for different noise levels. Three noise levels are displayed with $r = 0.1, 0.5$, and 1. For each case, the left box plot (hatched) corresponds to the initial positions/amplitudes and the right box plot (solid) corresponds to the refined positions/amplitudes. Note that the estimated amplitudes were scaled by r^{-1} to compare with the same ground-truth. For the box plots of the localization error after refinement (solid), we set the upper whiskers to 50 nm so as to consider any larger error as outliers. This is in line with the expected 3D localization error in SMLM [6]. This bound is not relevant for the initial errors (hatched) as they are too large. For the hatched box plots, we thus set the default upper whiskers to $Q3 + 1.5\text{IQR}$, where $\text{IQR} = (Q3 - Q1)$ is the interquartile range and $Q1, Q3$ are the 25th and 75th percentile, respectively. Finally, the lower whiskers are always set to the smallest error among all molecules. Outliers are indicated by \times .

5. Discussion

We have presented a joint-optimization framework to estimate both the RI map and the position of fluorescent molecules from an SMLM acquisition stack. Our method takes advantage of the sample-induced aberrations to unveil the map of the refractive index of the sample. Such structural information complements fluorescence imaging [10]. In addition to this unique feature, our framework is able to improve the accuracy of molecule localization. Our work shows that additional information about the sample can be recovered from SMLM data. This is a first step towards an exciting and new extension of SMLM. As future refinement, we need to look into ways to identify and correct the molecules that our framework can sometimes fail to refine. We shall then be in a good position to apply our framework to real data.

Declaration of competing interest

The authors declare that they have no known competing financial interests or personal relationships that could have appeared to influence the work reported in this paper.

Acknowledgments

T.-a.P. and M.U. were supported by the European Research Council (ERC) under the European Unions Horizon 2020 research and innovation programme (Grant Agreement No. 692726 GlobalBioIm). E.S. was supported by the LabEx CIMI, France (ANR-11-LABX-0040).

References

- [1] E. Betzig, G.H. Patterson, R. Sougrat, O.W. Lindwasser, S. Olenych, J.S. Bonifacio, M.W. Davidson, J. Lippincott-Schwartz, H.F. Hess, Imaging intracellular fluorescent proteins at nanometer resolution, *Science* 313 (5793) (2006) 1642–1645.
- [2] S.T. Hess, T.P. Girirajan, M.D. Mason, Ultra-high resolution imaging by fluorescence photoactivation localization microscopy, *Biophys. J.* 91 (11) (2006) 4258–4272.
- [3] M.J. Rust, M. Bates, X. Zhuang, Sub-diffraction-limit imaging by stochastic optical reconstruction microscopy (STORM), *Nat. Methods* 3 (10) (2006) 793–796.
- [4] B. Huang, W. Wang, M. Bates, X. Zhuang, Three-dimensional super-resolution imaging by stochastic optical reconstruction microscopy, *Science* 319 (5864) (2008) 810–813.
- [5] S.R.P. Pavani, M.A. Thompson, J.S. Biteen, S.J. Lord, N. Liu, R.J. Twieg, R. Piestun, W. Moerner, Three-dimensional, single-molecule fluorescence imaging beyond the diffraction limit by using a double-helix point spread function, *Proc. Natl. Acad. Sci.* 106 (9) (2009) 2995–2999.
- [6] D. Sage, T.-a. Pham, H. Babcock, T. Lukes, T. Pengo, J. Chao, R. Velmurugan, A. Herbert, A. Agrawal, S. Colabrese, A. Wheeler, A. Archetti, B. Rieger, R. Ober, G.M. Hagen, J.-B. Sibarita, J. Ries, R. Henriques, M. Unser, S. Holden, Super-resolution light club: Assessment of 2D and 3D single-molecule localization microscopy software, *Nat. Methods* 16 (5) (2019) 387–395.
- [7] H.P. Babcock, X. Zhuang, Analyzing single molecule localization microscopy data using cubic splines, *Sci. Rep.* 7 (1) (2017) 1–9.
- [8] Y. Li, M. Mund, P. Hoess, J. Deschamps, U. Matti, B. Nijmeijer, V.J. Sabinina, J. Ellenberg, I. Schoen, J. Ries, Real-time 3D single-molecule localization using experimental point spread functions, *Nat. Methods* 15 (5) (2018) 367–369.
- [9] F. Xu, D. Ma, K.P. MacPherson, S. Liu, Y. Bu, Y. Wang, Y. Tang, C. Bi, T. Kwok, A.A. Chubykin, P. Yin, S. Calve, G.E. Landreth, F. Huang, Three-dimensional nanoscopy of whole cells and tissues with in situ point spread function retrieval, *Nat. Methods* 17 (5) (2020) 531–540.
- [10] Y. Park, C. Depeursinge, G. Popescu, Quantitative phase imaging in biomedicine, *Nat. Photonics* 12 (10) (2018) 578–589.
- [11] Y. Xue, L. Waller, Computational hybrid imaging, 2020, arXiv preprint arXiv:2011.11574.
- [12] A.C. Gilbert, H.W. Levinson, J.C. Schotland, Imaging from the inside out: Inverse scattering with photoactivated internal sources, *Opt. Lett.* 43 (12) (2018) 3005–3008.
- [13] T.-a. Pham, E. Soubies, F. Soulez, M. Unser, Diffraction tomography from single-molecule localization microscopy: Numerical Feasibility, in: IEEE International Symposium on Biomedical Imaging, Nice, France, 2021.
- [14] E. Wolf, Three-dimensional structure determination of semi-transparent objects from holographic data, *Opt. Commun.* 1 (4) (1969) 153–156.
- [15] J.W. Goodman, Introduction To Fourier Optics, Roberts and Company Publishers, 2005.
- [16] A. Cornea, P.M. Conn, Fluorescence Microscopy: Super-Resolution and Other Novel Techniques, Elsevier, 2014.
- [17] H.-Y. Liu, D. Liu, H. Mansour, P.T. Boufounos, L. Waller, U.S. Kamilov, SEAGLE: Sparsity-driven image reconstruction under multiple scattering, *IEEE Trans. Comput. Imaging* 4 (1) (2017) 73–86.
- [18] E. Soubies, T.-a. Pham, M. Unser, Efficient inversion of multiple-scattering model for optical diffraction tomography, *Opt. Express* 25 (18) (2017) 21786–21800.
- [19] T.-a. Pham, E. Soubies, A. Ayoub, J. Lim, D. Psaltis, M. Unser, Three-dimensional optical diffraction tomography with Lippmann-Schwinger model, *IEEE Trans. Comput. Imaging* 6 (2020) 727–738.
- [20] A. Aristov, B. Lelandaïs, E. Rensen, C. Zimmer, ZOLA-3D allows flexible 3D localization microscopy over an adjustable axial range, *Nature Commun.* 9 (1) (2018) 1–8.
- [21] S. Liu, E.B. Kromann, W.D. Krueger, J. Bewersdorf, K.A. Lidke, Three dimensional single molecule localization using a phase retrieved pupil function, *Opt. Express* 21 (24) (2013) 29462–29487.
- [22] M.F. Juette, T.J. Gould, M.D. Lessard, M.J. Mlodzianowski, B.S. Nagpure, B.T. Bennett, S.T. Hess, J. Bewersdorf, Three-dimensional sub-100 nm resolution fluorescence microscopy of thick samples, *Nat. Methods* 5 (6) (2008) 527–529.
- [23] L.I. Rudin, S. Osher, E. Fatemi, Nonlinear total variation based noise removal algorithms, *Physica D* 60 (1–4) (1992) 259–268.
- [24] S. Lefkimmatis, J.P. Ward, M. Unser, Hessian schatten-norm regularization for linear inverse problems, *IEEE Trans. Image Process.* 22 (5) (2013) 1873–1888.
- [25] G. Ongie, A. Jalal, C.A. Metzler, R.G. Baraniuk, A.G. Dimakis, R. Willett, Deep learning techniques for inverse problems in imaging, *IEEE J. Sel. Areas Inf. Theory* 1 (1) (2020) 39–56.
- [26] F. Yang, T.-a. Pham, H. Gupta, M. Unser, J. Ma, Deep-learning projector for optical diffraction tomography, *Opt. Express* 28 (3) (2020) 3905–3921.
- [27] H. Gupta, K.H. Jin, H.Q. Nguyen, M.T. McCann, M. Unser, CNN-based projected gradient descent for consistent CT image reconstruction, *IEEE Trans. Med. Imaging* 37 (6) (2018) 1440–1453.
- [28] A. Goy, G. Rughoobur, S. Li, K. Arthur, A.I. Akinwande, G. Barbastathis, High-resolution limited-angle phase tomography of dense layered objects using deep neural networks, *Proc. Natl. Acad. Sci.* 116 (40) (2019) 19848–19856.
- [29] S. Kullback, R.A. Leibler, On information and sufficiency, *Ann. Math. Stat.* 22 (1) (1951) 79–86.
- [30] M. Zehni, L. Donati, E. Soubies, Z. Zhao, M. Unser, Joint angular refinement and reconstruction for single-particle cryo-EM, *IEEE Trans. Image Process.* 29 (2020) 6151–6163.
- [31] M. Xie, Y. Sun, J. Liu, B. Wohlberg, U.S. Kamilov, Joint reconstruction and calibration using regularization by denoising, 2020, arXiv preprint arXiv:2011.13391.
- [32] E. Soubies, F. Soulez, M.T. McCann, T.-a. Pham, L. Donati, T. Debarre, D. Sage, M. Unser, Pocket guide to solve inverse problems with GlobalBioIm, *Inverse Problems* 35 (10) (2019) 1–20.
- [33] P. Wolfe, Convergence conditions for ascent methods, *SIAM Rev.* 11 (2) (1969) 226–235.
- [34] L. Armijo, Minimization of functions having Lipschitz continuous first partial derivatives, *Pacific J. Math.* 16 (1) (1966) 1–3.
- [35] L. Tian, L. Waller, 3D Intensity and phase imaging from light field measurements in an LED array microscope, *Optica* 2 (2) (2015) 104–111.
- [36] T.-a. Pham, E. Soubies, A. Goy, J. Lim, F. Soulez, D. Psaltis, M. Unser, Versatile reconstruction framework for diffraction tomography with intensity measurements and multiple scattering, *Opt. Express* 26 (3) (2018) 2749–2763.
- [37] Y. Ma, H. Mansour, D. Liu, P.T. Boufounos, U.S. Kamilov, Accelerated image reconstruction for nonlinear diffractive imaging, in: 2018 IEEE International Conference on Acoustics, Speech and Signal Processing, ICASSP, Calgary AB, Canada, 2018, pp. 6473–6477.
- [38] Y. Nesterov, Gradient methods for minimizing composite functions, *Math. Program.* 140 (1) (2013) 125–161.
- [39] A. Beck, M. Teboulle, A fast iterative shrinkage-thresholding algorithm for linear inverse problems, *SIAM J. Imaging Sci.* 2 (1) (2009) 183–202.
- [40] A. Beck, M. Teboulle, Fast gradient-based algorithms for constrained total variation image denoising and deblurring problems, *IEEE Trans. Image Process.* 18 (11) (2009) 2419–2434.
- [41] L. Tian, X. Li, K. Ramchandran, L. Waller, Multiplexed coded illumination for Fourier ptychography with an LED array microscope, *Biomed. Opt. Express* 5 (7) (2014) 2376–2389.
- [42] J. Min, S.J. Holden, L. Carlini, M. Unser, S. Manley, J.C. Ye, 3D high-density localization microscopy using hybrid astigmatic/biplane imaging and sparse image reconstruction, *Biomed. Opt. Express* 5 (11) (2014) 3935–3948.
- [43] Z. Wang, A.C. Bovik, H.R. Sheikh, E.P. Simoncelli, Image quality assessment: From error visibility to structural similarity, *IEEE Trans. Image Process.* 13 (4) (2004) 600–612.
- [44] R.E. Thompson, D.R. Larson, W.W. Webb, Precise nanometer localization analysis for individual fluorescent probes, *Biophys. J.* 82 (5) (2002) 2775–2783.
- [45] J. Chao, E.S. Ward, R.J. Ober, Fisher Information theory for parameter estimation in single molecule microscopy: Tutorial, *J. Opt. Soc. Amer. A* 33 (7) (2016) B36–B57.